

# Deposition of Ingested Volcanic Ash on Surfaces in the Turbine of a Small Jet Engine\*\*

By Maya Shinozaki, Kevin A. Roberts, Bennie van de Goor and T. William Clyne\*

There is ongoing demand for increased turbine entry temperatures, and hence improved engine efficiency. This applies to both power generation turbines and those used for propulsion (aero and marine). Ingested particulate, such as sand, fly ash, and volcanic ash (VA), often referred to generically as calcia–magnesia–alumina–silica (CMAS), can cause significant problems in both types of turbine. Such particles may melt, or at least soften, in flight, making it more likely that they will adhere to surfaces within the turbine on impact. Increased turbine entry temperatures clearly raise the danger of this happening. Particulate CMAS from volcanoes, provided it does adhere (rather than simply passing through the engine), can be quite severely deleterious in aeroengines.<sup>[1]</sup> Such ash can be more erosive, and have a significantly lower melting point, compared to conventional air borne dust.<sup>[2]</sup> In the combustion chamber, where the flame temperature may be as high as 1650 °C, silica-based slag deposits have been observed to plug combustor liner cooling holes, thus creating hot spots that can lead to premature failure.<sup>[3]</sup> Deposits can also form on blade surfaces and along nozzle guide vanes, causing local overheating.<sup>[4]</sup> Both erosion and deposition are known to increase levels of surface roughness, which produces corresponding increases in heat transfer (up to 50%) and skin friction (up to 300%).<sup>[5]</sup> Among the most important parameters determining the level of deposition are the gas (and particle) temperature and also the turbine surface temperature.<sup>[5,6]</sup> The particle temperature at the end of its flight determines its physical state, which in turn influences whether it will cause erosion upon impact or deposition. Lower deposition levels were observed in areas with reduced turbine surface temperature.<sup>[7]</sup> Experiments conducted by Crosby *et al.*,<sup>[6]</sup> using an accelerated deposition facility, showed that larger and

hotter particles are more likely to deposit and hotter surfaces are more successful in capturing impinging particulate.

Furthermore, CMAS deposits are known to cause accelerated degradation of ceramic coatings on such components. For example, yttria-partially stabilized zirconia (YSZ) coatings can be damaged by at least two types of mechanism. If CMAS deposits are heated sufficiently, their viscosity can become low enough for them to infiltrate the (porosity in the) YSZ, causing a dramatic loss in its strain tolerance and leading to spallation.<sup>[8–14]</sup> Secondly, chemical interaction can occur between CMAS and the YSZ, for example so as to cause the YSZ to dissolve into the CMAS melt and re-precipitate yttria-lean zirconia grains. These grains are prone to transform to the monoclinic phase on cooling,<sup>[15,16]</sup> and the associated volume change (3–4%) may be sufficient to drive microcracks and cause failure.<sup>[17,18]</sup>

There is thus considerable interest in identifying and quantifying the factors affecting the likelihood of ingested particles adhering to surfaces within the turbine, since it is clear that such adhesion can rapidly lead to severe degradation. Rather surprisingly, there appear to be very few reports in the open literature of such experimental work with a gas turbine, although there is naturally quite extensive in-service experience and there have also been studies of deposition efficiencies using various test facilities.<sup>[5,6,19]</sup> However, the conditions within such set-ups are likely to be different from those created during ingestion into a real gas turbine engine. The current study is focussed on such a study, involving the ingestion of VA into a small turbojet engine and subsequently using an optical fiber viewing system to examine the interior of the turbine. A simple numerical model is employed to give some insights into particle thermal and displacement histories during flight.

[\*] T. W. Clyne, M. Shinozaki, K. A. Roberts

Department of Materials Science and Metallurgy, Cambridge University, Pembroke Street, Cambridge CB2 3QZ, UK  
E-mail: [twc10@cam.ac.uk](mailto:twc10@cam.ac.uk)

B. van de Goor

AMT Netherlands b.v., Spaarpot 34, 5667 KX Geldrop, The Netherlands

[\*\*] Funding for this work has come from a Schools Competition Act Settlement Trust (SCAST) Research Scholarship and the Royal Aeronautical Society Centennial Research Scholarship. Thanks are due to Dr. Margaret Hartley of the Earth Sciences Department in Cambridge University for the provision of the volcanic ash specimen.

## 1. Experimental

### 1.1. Powder Characterization

The original VA material was obtained (via Dr. Margaret Hartley of the Earth Sciences Department in Cambridge University) by extraction from the ground near the Laki vent in Southern Iceland. It was subjected to a grinding operation in a rotary mill and then sieved to give four selected ranges of size. The chemical composition, obtained from EDX data, is shown in Table 1. It can be seen that the ash contains a number of elements at significant levels, and is particularly rich in Si and Fe.

The phase constitution of the powder was investigated via X-ray diffraction data obtained using a Philips PW1710

Table 1. Elemental composition of the VA powder, obtained by EDX analysis.

Element	Weight (%)
O	Bal.
Na	1
Mg	2
Al	6.7
Si	24
K	0.1
Ca	6.1
Ti	2.4
Fe	21.3

diffractometer, with Cu K $\alpha$  radiation ( $\lambda = 0.154$  nm), 40 kV accelerating current and a 40 mA filament current. The XRD profile is shown in Figure 1, where it can be seen that four crystalline phases have been identified, mostly at relatively low levels. These correspond to albite (sodium aluminum silicate), enstatite (magnesium silicate), sanidine (potassium sodium aluminum silicate) and magnetite (iron oxide). Albite is a plagioclase feldspar mineral, common in granitic rocks. Enstatite is commonly found in igneous and metamorphic rocks. Sanidine is a potassium feldspar, usually found in volcanic rocks. Finally, magnetite is one of the most common naturally occurring iron oxides. It is important to note, however, that there is a prominent broad peak at around 20–30°(2 $\theta$ ), clearly indicating that a substantial proportion of amorphous phase is present. The amorphous and crystalline phase proportions were calculated after peak deconvolution and profile fitting, performed using Phillips PROFIT software. The amorphous proportion of the VA sample was estimated to be around 80–90%.

The glass transition temperature and melting point of the VA were obtained using a Netzsch 404 High Temperature DSC. The DSC signal was obtained using a ramp rate of 10 °C min<sup>-1</sup>

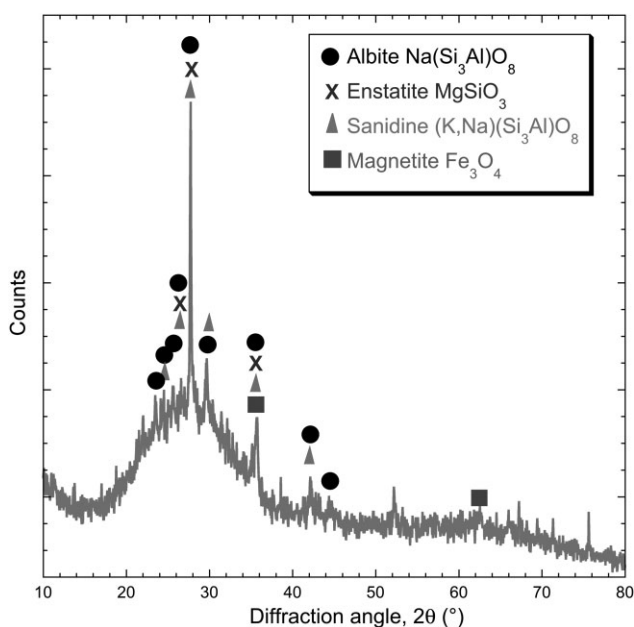


Fig. 1. X-ray diffraction profile of the VA powder.

up to 1500 °C. A DSC plot (for the sample having an average particle size of 20 μm) is shown in Figure 2. It can be seen that the glass transition temperature,  $T_g$  (above which the amorphous fraction softens dramatically) is around 600–700 °C and the melting point,  $T_m$  (temperature at which the crystalline component melts) is about 1130 °C. Of course, the concept of a  $T_m$  value is dubious in this case, since there is only a small crystalline content and that is apparently made up of several phases. Nevertheless, it is worth noting that some sort of melting event does apparently occur at around 1100–1200 °C. Probably the most significant point to register at this stage is that the powder has a high amorphous content and that its  $T_g$  value is low ( $\approx 600$  °C). The specific heat capacity was measured to be approximately 800 J kg<sup>-1</sup> K<sup>-1</sup>. The heat capacity calibration constant, required in order to determine the absolute heat flow, was measured using a sapphire standard.

Particle size distributions for the four different sieve fractions were obtained using a Malvern P580 Mastersizer E. Particles were mixed in an aqueous solution and kept in suspension using a stirrer. A laser beam passes through the suspension and a detector measures the intensity of scattered light, giving the particle size distribution. The distributions are shown in Figure 3, for fractions designated as “fine”, “medium 1”, “medium 2” and “coarse”. The average diameters in these cases were approximately 20, 50, 75, and 100 μm, respectively. (It has been reported<sup>[19,20]</sup> that the maximum size of particles ingested into a jet engine is typically about 100 μm.) Particle morphologies were examined using a JEOL-5800 SEM, with a typical accelerating voltage of 10–15 kV. Samples were sputter coated with gold (using an Emitech 330 facility), to prevent charging. Typical morphologies were observed to be angular and irregular – see Figure 4. It was assumed that both chemical composition and thermal properties ( $T_g$  and  $T_m$ ) do not vary widely between the different particle size fractions, and therefore were taken to be constant, especially as the

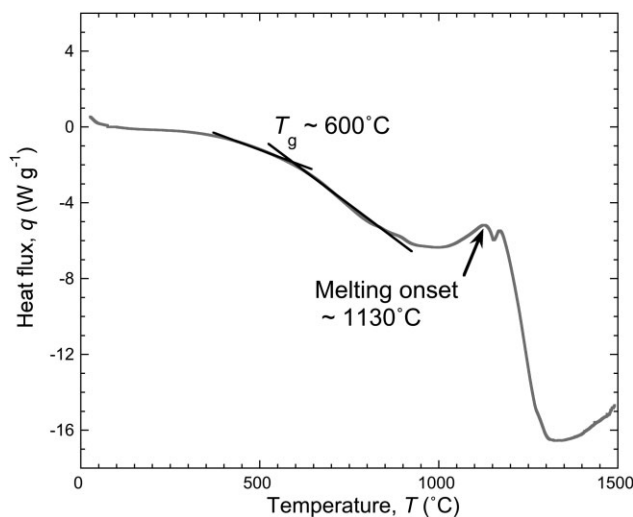


Fig. 2. DSC plot from a VA sample (with an average particle size of 20 μm), obtained using a heating rate of 10 K min<sup>-1</sup>.

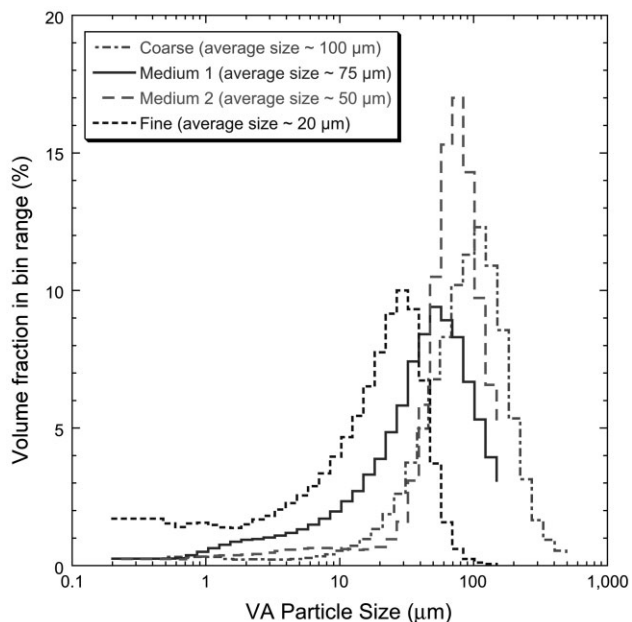


Fig. 3. Particle size distributions of VA powders (fine, medium 1, medium 2, and coarse), with the bin ranges indicated by the widths of the histogram columns.

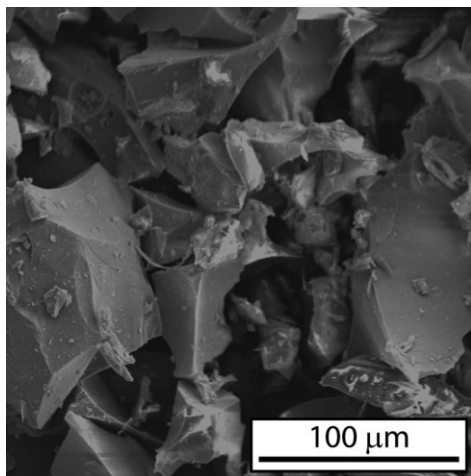


Fig. 4. SEM image of VA powder.

amorphous fraction of the bulk VA powder was already very high at around 80–90%. The chemical composition and, particularly, the amorphous/crystalline fractions of the VA may in practice vary slightly with particle size. (In view of the explosive processes by which VA is produced, finer particles may be subjected to more rapid cooling and possibly to greater mechanical damage.) However, such factors are unlikely to affect significantly the conclusions of the present type of study.

### 1.2. Operation of the Turbojet Engine

The type of engine employed in this work was a Pegasus HP E-Start engine, supplied by AMT Netherlands. It is a turbojet engine, with no by-pass air flow. The main technical

specifications and operational parameters are shown in Table 2. The data presented refer to runs carried out with throttle settings at 100 and 50%, corresponding to engine speeds of around 120 000 and 62 000 rpm, respectively. The complete experimental set-up is shown in Figure 5a, with the engine mounted horizontally, the intake facing the camera and the exhaust pointing towards the extraction unit in the wall. The powder feeding system comprised a Dreschel bottle, containing the VA powder, with the inlet connected to a compressed air line and the outlet secured on a clamp, so that the ash was fed more or less axially into the intake. Compressed air entered the Dreschel bottle via the inlet, which then swirled the VA around, eventually pushing the particles out through the outlet. The feed rate was controlled by adjusting the pressure of the compressed air line.

The interior of the engine concerned was examined after each run, using a 5.5 mm diameter rigid borescope with 90° direction and 55° field of view (Inspection Optics Ltd.). The endoscope had a focusing eyepiece and was connected to a 24 W light source, and an SLR camera, in order to capture the images.

## 2. Numerical Modeling of Particle Acceleration and Heating

### 2.1. Particle Motion

Particle acceleration and heating were modeled in a 1-D Lagrangian (convected coordinates) frame of reference. Particles are assumed to move predominantly under the influence of the drag force exerted by the gas,  $F_{\text{drag}}$ , so that particle location is determined by the following equations:<sup>[21,22]</sup>

$$\frac{dx_p}{dt} = U_p \quad (1)$$

$$\frac{m_p dU_p}{dt} = F_{\text{drag}} = \frac{\rho_f A (U_\infty - U_p)^2 C_D}{2} \quad (2)$$

where  $x_p$  is the particle displacement,  $m_p$  is the particle mass,  $U_p$  is the particle velocity,  $A$  is the particle frontal area,  $C_D$  is the drag coefficient,  $\rho_f$  is the carrier fluid (gas) density and  $U_\infty$  the free stream velocity. The following assumptions are also made:

- Particles are rigid spheres
- Gas flow is laminar

Table 2. Operational parameters for the jet engine.

Parameter	Engine speed (rpm)	
	120 000	62 000
Engine diameter (mm)	120	
Engine length (mm)	342	
Combustion chamber length (mm)	100	
Engine weight (kg)	2.225	
Fuel type	Kerosene	
Measured thrust (N)	141	22
Pressure ratio	3.2:1	2.9:1
Air mass flow rate ( $\text{kg s}^{-1}$ )	0.375	0.185
Fuel consumption ( $\text{kg s}^{-1}$ )	0.0081	0.0025
Exhaust gas temperature ( $^{\circ}\text{C}$ )	600	480

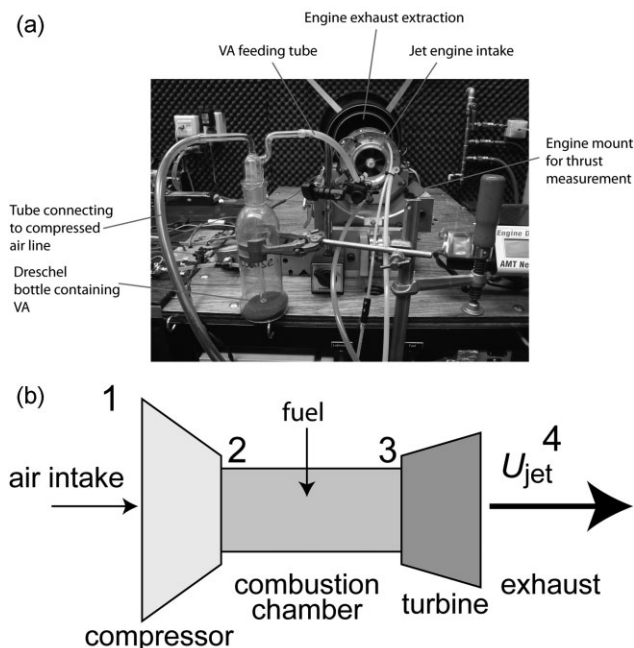


Fig. 5. (a) Photograph of the experimental set-up and (b) schematic of engine regimes.

- The density of the particulate is much higher than that of the gas ( $\rho_p \gg \rho_f$ ).

Under these conditions, the particle equation of motion reduces to:

$$\frac{dU_p}{dt} = \frac{3}{4} \frac{\rho_f C_D}{\rho_p D_p} (U_\infty - U_p)^2 \quad (3)$$

where  $D_p$  is the particle diameter and  $\rho_p$  the particle density. A constant value of 0.5 was used for  $C_D$ , which is typical for a sphere at high Reynolds numbers (of the order of  $10^3$ ). The particle Reynolds number,  $Re_p$  is given by:

$$Re_p = \frac{\rho_f D_p |U_\infty - U_p|}{\mu_g} \quad (4)$$

where  $U_\infty$  is the velocity of the gas and  $\mu_g$  is its dynamic viscosity.

The Stokes number (ratio of characteristic time for particle velocity change to that for fluid flow over an obstacle) can be expressed in this case as

$$Stk = \frac{\tau U_\infty}{D_p} \approx \frac{\rho_p D_p^2 U_\infty}{18 \mu_g D_o} \quad (5)$$

where  $D_o$  is the characteristic dimension of the obstacle

## 2.2. Particle Heating

The particle was taken to be isothermal throughout (i.e. Newtonian cooling conditions), initially at temperature  $T_0$ , and surrounded throughout by gas at  $T_\infty$ . The equation describing

convective heat exchange between gas and particle may be written:

$$Q = m_p c_{p,p} \frac{dT_p}{dt} = h S_p (T_\infty - T_p) \quad (6)$$

where  $Q$  is the heat flux,  $h$  is the convective heat transfer coefficient,  $c_{p,p}$  is the specific heat capacity of the particle,  $T_p$  is the particle temperature and  $S_p$  is the particle surface area. By expressing  $S_p$  and  $m_p$  in terms of  $D_p$  and  $\rho_p$ , the following equation is obtained:

$$\frac{dT_p}{dt} = \frac{6h}{\rho_p c_{p,p} D_p} (T_\infty - T_p) \quad (7)$$

Radiation is unlikely to have a significant effect over the temperature range of interest here and has hence been neglected. The heat transfer coefficient was estimated, as a function of the relative velocity between particle and surrounding gas, using the Ranz–Marshall correlation for the Nusselt number:

$$\frac{h D_p}{k_f} = Nu = 2.0 + 0.6 Re_p^{1/2} Pr^{1/3} \quad (8)$$

where  $k_f$  is the thermal conductivity of the gas and  $Pr$  is its Prandtl number, given by

$$Pr = \frac{c_f \mu_f}{k_f} \quad (9)$$

where  $c_f$  is the specific heat capacity of air and generally,  $Pr$  has a value of about  $\approx 0.70$  for air. Typical values for the heat transfer coefficient calculated in this study were in the approximate range  $10\text{--}30 \text{ kW m}^{-2} \text{ K}^{-1}$ .

The input data used in the model are listed in Table 3. The free stream gas velocity was assumed to be equal to the calculated jet speed. The jet speed was evaluated from the (measured) gross thrust,  $F_G$ , which is related to the inlet air mass flow rate,  $(dm_{\text{air}}/dt)$ , and the fuel consumption rate,  $(dm_{\text{fuel}}/dt)$ .

$$F_G = \left[ \frac{dm_{\text{air}}}{dt} + \frac{dm_{\text{fuel}}}{dt} \right] U_{\text{jet}} \quad (10)$$

The far field gas temperature was assumed to be equal to the calculated turbine entry temperature, corresponding to the temperature at location 3 ( $T_3$ ) in the schematic of a simple gas turbine engine, shown in Figure 5b. This was evaluated assuming isentropic compression across the compressor (from the pressure ratios in Table 2) and using the perfect gas relationship:

$$\frac{T}{p^{(\gamma-1)/\gamma}} = \text{const.} \quad (11)$$

where  $p$  and  $T$  are the gas pressure and temperature, and  $\gamma$  is the ratio of the specific heat capacities of air (taken to be equal to 1.4 in this case). The combustion process was modeled as

Table 3. Input parameters for particle acceleration and heating model.

Parameter	Engine speed (rpm)	
	120 000	62 000
Free stream velocity, $U_\infty$ ( $\text{m s}^{-1}$ )	365	115
Far field gas temperature, $T_\infty$ ( $^\circ\text{C}$ )	1070	710
Air density at $T_3$ and $p_3$ , $\rho_f$ ( $\text{kg m}^{-3}$ )	0.84	1.04
Air dynamic viscosity at $T_3$ , $\mu_f$ ( $\text{kg s}^{-1} \text{m}^{-1}$ )	$4.4 \times 10^{-5}$	$4.0 \times 10^{-5}$
Air Prandtl number, $Pr_f$	0.70	0.71
Air thermal conductivity at $T_3$ , $k_f$ ( $\text{W m}^{-1} \text{K}^{-1}$ )	0.08	0.06
Particle density, $\rho_p$ ( $\text{kg m}^{-3}$ ) <sup>[23]</sup>		2400
Particle thermal conductivity, $k_p$ ( $\text{W m}^{-1} \text{K}^{-1}$ )		2
Particle specific heat capacity, $c_{p,p}$ ( $\text{J kg}^{-1} \text{K}^{-1}$ )		800
Initial particle velocity, $U_0$ ( $\text{m s}^{-1}$ )		0
Initial particle temperature, $T_0$ ( $^\circ\text{C}$ )		20
Drag coefficient, $C_D$ (-)		0.5

reversible and isobaric. The fluid (air) was modeled as an ideal gas throughout the cycle. The steady flow energy equation was used to evaluate the rate of heat release for the combustion process:

$$Q_{\text{combust}} = \frac{dm_{\text{air}}}{dt} c_{p,\text{air}}(T_3 - T_2) = \frac{dm_{\text{fuel}}}{dt} H_{\text{fuel}} \quad (12)$$

where  $T_4$  is the exhaust gas temperature (see Figure 5b),  $c_{p,\text{air}}$  is the specific heat capacity of air (taken to be  $1005 \text{ J kg}^{-1} \text{ K}^{-1}$ ) and  $H_{\text{fuel}}$  is the calorific value of the kerosene (taken to be  $43 \text{ MJ kg}^{-1}$ ).

Finally, the following finite difference equations were used in order to solve Eqs. (1), (3), and (7) numerically, using Euler's method:

$$x_p^{n+1} = U_p^n \Delta t \quad (13)$$

$$U_p^{n+1} = \frac{3 \rho_f C_D}{4 \rho_p D_p} (U_\infty - U_p^n)^2 \Delta t \quad (14)$$

$$T_p^{n+1} = \frac{6h}{\rho_p c_{p,p} D_p} (T_\infty - T_p^n) \Delta t \quad (15)$$

where  $\Delta t$  is the time step used in order to conduct the iteration. A value of  $10^{-7} \text{ s}$  was used, which gave adequate accuracy and stability of the modeling results.

The validity of the assumption of Newtonian cooling conditions (i.e. the particles are isothermal throughout) was checked for all cases studied by evaluating the Biot number

( $Bi = hD_p/k_p$ ), which needs to be well below unity for this to be a reliable approximation. The  $Bi$  values obtained were in the range 0.17–0.32, which is considered acceptable in the context of (order of magnitude) calculations of the type being carried out here.

The Stokes number, as obtained using Eq. (5), and taking the free stream velocity to be  $365 \text{ m s}^{-1}$ , particle density to be  $2400 \text{ kg m}^{-3}$ , gas viscosity to be  $4.4 \times 10^{-5} \text{ kg s}^{-1} \text{ m}^{-1}$  and obstacle dimension to be 10 mm, has a value of about 1000 (representing a strong tendency to deviate from the gas streamlines) for a particle diameter of  $100 \mu\text{m}$ , but a value of about 0.1 (representing a strong tendency to follow streamlines) for a particle diameter of  $1 \mu\text{m}$ .

### 3. Powder Injection and Deposition

#### 3.1. Observed Deposition Behavior

Experimental parameters and deposition observations are summarized in Table 4. No deposition was observed when the engine was running at 62 000 rpm. The estimated turbine entry temperature in this case was  $710 \text{ }^\circ\text{C}$ . However, at 120 000 rpm, for which the turbine entry temperature was estimated to be  $1070 \text{ }^\circ\text{C}$ , deposition was observed to be extensive in several cases.

Figure 6 shows images obtained using the borescope for the higher engine speed. There was no deposition on rotor blades and the images all show nozzle guide vanes and nearby blade platforms. They are organized in increasing order of "Damage Level" to the engine, the key for which is shown in Table 5. Figure 6a, which is from run A (see Table 4), indicates that there was relatively little deposition with the fine VA, although some did collect on one or two nozzle guide vanes. Figure 6b, relating to run D, which involved "medium 1" powder, shows that there was rather more deposition in this case, although it was still restricted to only a few locations. It is noticeable in both of these images, and more generally, that locations where some particle adhesion occurs subsequently tend to exhibit build-ups of deposition – i.e. the prior presence of adhered particles promotes further adhesion. Of course, this can be explained in terms of increased roughness raising the likelihood of impact leading to adhesion.

Table 4. Summary of run conditions and corresponding adhesion observations.

Run code	VA grade	Engine speed (rpm)	VA feed rate ( $\text{g min}^{-1}$ )	Duration (s)	VA injected (g)	VA concentration ( $\text{g m}^{-3}$ )	Engine damage level
A	Fine	120 000	10.9	110	20	0.59	1
B	Medium 1	120 000	6.7	90	10	0.36	0
C	Medium 1	120 000	15	180	45	0.82	5
D	Medium 1	120 000	24	50	20	1.31	2
E	Medium 2	120 000	41.9	43	30	2.28	3
F	Coarse	120 000	2	30	1	0.11	0
G	Coarse	120 000	30	60	30	1.63	4
H	Fine	62 000	15.4	78	20	1.7	0
I	Fine	62 000	32.4	37	20	3.58	0
J	Medium 1	62 000	23.1	52	20	2.55	0

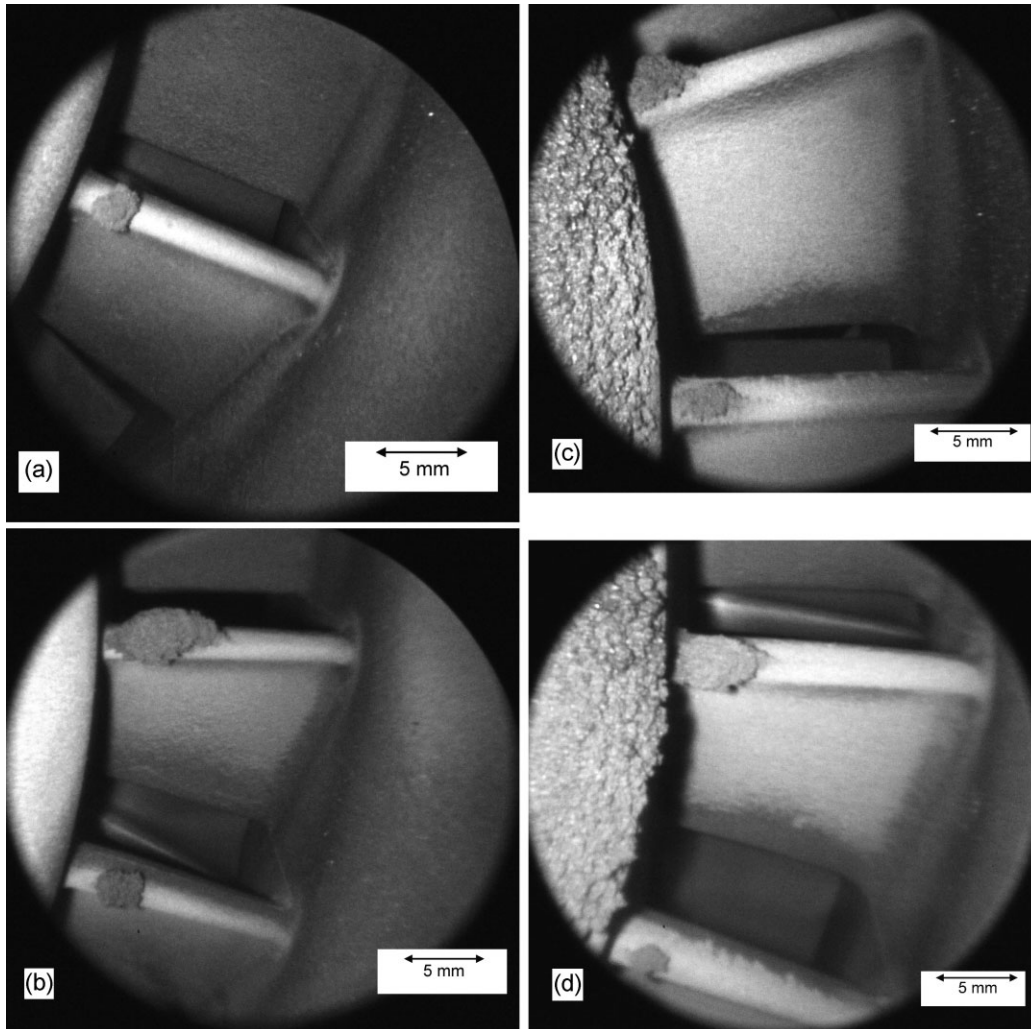


Fig. 6. Borescope images from (a) run A, (b) run D, (c) run E, and (d) run G.

Figure 6c relates to a run E involving “medium 2” particle size, and the injection of more powder than in runs A and D. It can be seen that deposition is now more substantial, and extends to a larger proportion of the available surface, demonstrating that coarser particles deposit more effectively, and that this deposition is progressive. Finally, Figure 6d indicates that extensive deposition also occurred with the coarsest powder (100  $\mu\text{m}$ ). The damage characteristics exhibited after all of these runs are summarized in Figure 7, which

indicates that more deposition occurred with the coarser particles, and that in all cases the deposition was progressive with continued injection of powder.

### 3.2. Correlation with Modeled Impact Characteristics

Predicted particle displacement and thermal histories (for an engine speed of 120 000 rpm) are shown in Figure 8 and 9, for all four particle sizes. Assuming a flight distance (combustion chamber length) of 100 mm, the time of flight

Table 5. Engine damage level key.

Engine damage level	Description
0	No deposition
1	Very small amounts deposition on blades and combustion chamber wall
2	Larger lumps of deposition on blades and combustion chamber wall
3	Film deposition observed over a significant area (over 50%) of the combustion chamber wall
4	More deposition on blades leading edge and lumps deposited on combustion chamber wall exceed $\approx 1$ mm in height
5	Large amounts of deposition on blade surfaces (more than 50% of the blades were affected), film deposition all over the combustion chamber wall and overall engine performance was significantly reduced during the run

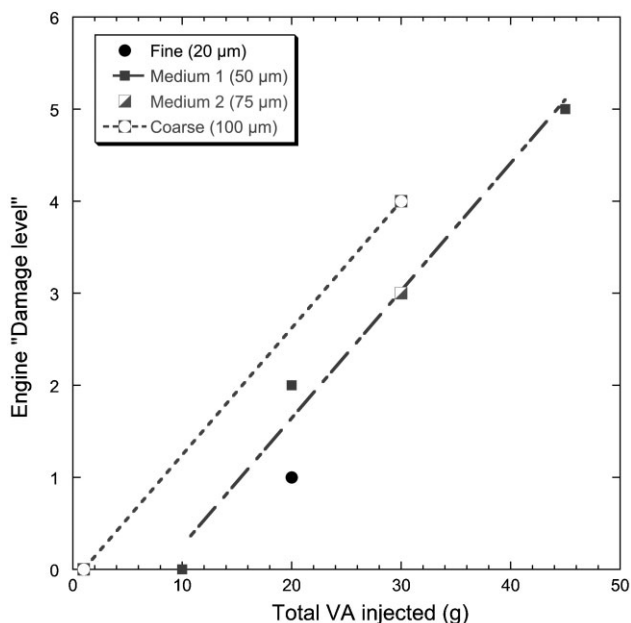


Fig. 7. Damage level index as a function of the total amount of VA injected, for the four particle sizes, with an engine speed of 120 000 rpm.

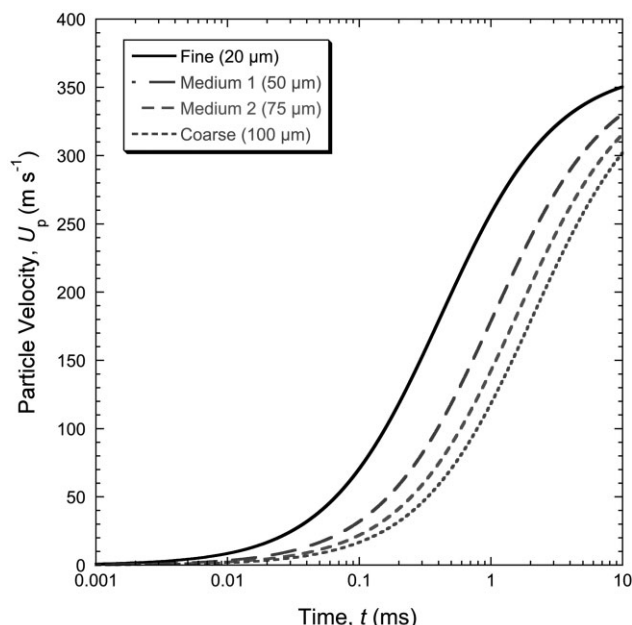


Fig. 8. Predicted particle velocity as a function of time, for a free stream velocity of 365 m s<sup>-1</sup> (the estimated value for an engine speed of 120 000 rpm).

and the particle temperature at the end of flight are shown in Table 6, for each particle size. Several features are apparent from these predictions. Firstly, as expected, smaller particles become appreciably hotter during flight. The fine particles reach virtually the gas combustion temperature (1070 °C) by the time they enter the turbine (after about 0.7 ms), whereas the coarsest particles (100 μm) have only reached about 400 °C by that point, despite the fact that this takes almost twice as long

(1.3 ms). Of course, while 1070 °C is well above  $T_g$  ( $\approx 600$  °C), and close to the melting temperature, 400 °C is appreciably below  $T_g$ . Secondly, the velocity of the finest particles at that point ( $\approx 226$  m s<sup>-1</sup>) is considerably higher than that of the coarsest particles ( $\approx 137$  m s<sup>-1</sup>).

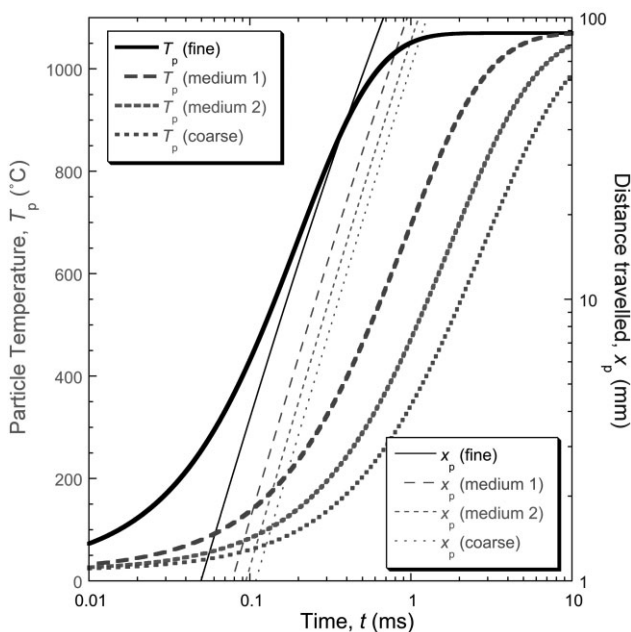


Fig. 9. Predicted particle temperature and displacement as a function of time, for a free stream velocity of 365 m s<sup>-1</sup> and a far field temperature of 1070 °C (estimated values for an engine speed of 120 000 rpm).

These modeling outcomes should now be considered in the context of the observation that the coarse particles seem to adhere much more readily than the finer ones. There are two points that should be noted here. Firstly, particle size is expected to have a strong influence on inertial behavior. Finer particles tend to follow gas streamlines, whereas larger ones may have sufficient inertia to ensure that they do not deflect with the gas flow when its direction changes sharply. Only when particles are not readily carried with the gas stream would they be likely to strike a component surface, and it may well be that the fine particles in these experiments did not do this. Secondly, while the coarse particles are predicted to be relatively cool on impact, the temperature of the substrates concerned (nozzle guide vanes) are expected to be well above this level (when the turbine entry temperature of the gas is above 1000 °C), and indeed, may well be above the  $T_g$  value of VA particles (which tends to be appreciably lower than that of other types of CMAS). Of course, in order to predict rigorously whether adhesion is expected, it would be necessary to model the impact and spreading phenomena, including the associated heat transfer. However, in general it seems plausible to suggest that particles of around 50–100 μm are moving fast enough, and have sufficient inertia, to strike these substrates on entering the turbine and that, when they do, their temperature, and that of the substrate, taking into account the (relatively low)  $T_g$  value of this VA, are such that they often soften sufficiently to spread and adhere on impact.

Table 6. Calculated time of flight values (assuming 100 mm long combustion chamber), and corresponding particle speed and temperatures, for VA particles (engine speed 120 000 rpm).

$D_p$	Time of flight (ms)	$U_p$ at end of flight ( $\text{m s}^{-1}$ )	$T_p$ at end of flight ( $^{\circ}\text{C}$ )
Fine (20 $\mu\text{m}$ )	0.68	226	1011
Medium 1 (50 $\mu\text{m}$ )	0.95	174	677
Medium 2 (75 $\mu\text{m}$ )	1.12	152	507
Coarse (100 $\mu\text{m}$ )	1.26	137	403

#### 4. Conclusions

The following conclusions can be drawn from this work.

- A small gas turbine engine has been used in order to investigate the deposition behavior of ingested VA powder. Two engine speeds (62 000 and 120 000 rpm) and four different particle size distributions of VA particles were used in the experiments, with average particle diameters of about 20, 50, 75, and 100  $\mu\text{m}$ . The powder had a  $T_g$  value of the order of 600  $^{\circ}\text{C}$ , with a substantial amorphous content, and a melting temperature around 1100  $^{\circ}\text{C}$ .
- No deposition was observed with the lower engine speed and also there was no deposition in any run on moving (rotor blade) surfaces. However, significant deposition on stationary surfaces (nozzle guide vanes and adjoining blade platform) was seen in several cases with the engine at full power. It was noticeable that substantially more deposition took place with the coarser particles than with the fine ones.
- A simple numerical model has been used to predict particle displacement and thermal histories within the combustion chamber and on entry to the turbine. At full power, the gas turbine entry temperature was estimated to be about 1070  $^{\circ}\text{C}$ . Fine particles (20  $\mu\text{m}$ ) are predicted to reach this temperature after flight through the combustion chamber, which takes <1 ms. The relatively limited deposition observed with them is therefore attributed to their inertia being low, so that they tend to be carried with the gas as it is deflected past solid surfaces and do not readily impact on them. These particles are predicted to be travelling at about 200–250  $\text{m s}^{-1}$  as they enter the turbine, with the surrounding gas stream velocity being about 350  $\text{m s}^{-1}$ . No systematic modeling has been attempted of the expected trajectories such particles will follow when the gas stream deviates around obstacles, but their Stokes number is estimated to be relatively low, suggesting that they will tend to follow the streamlines and hence avoid impact with solid surfaces.
- Larger particles (100  $\mu\text{m}$ ) are predicted to be no hotter than about 400  $^{\circ}\text{C}$ , which is below  $T_g$ , on entry to the turbine. However, their estimated Stokes number is much larger ( $\approx 1000$ ), indicating that their high inertia makes it likely that they will strike solid surfaces within

the turbine. These surfaces are themselves likely to be well above  $T_g$  as a result of heating by the gas stream, and the upshot of this is apparently that the particles commonly become soft enough to spread and adhere on impact. It is probable that particles much larger than this (e.g.  $\approx 200 \mu\text{m}$ ) would be too cold on impact for this to occur, although the present experimental study has been limited to particles of up to around 100  $\mu\text{m}$  diameter.

- While these experimental observations are qualitative, and the model used is relatively crude, the results appear to be consistent and to give at least some insights into the main phenomena involved. The main conclusion is that VA of this type, which often has a relatively low  $T_g$  and a large amorphous content, can exhibit a marked tendency to adhere to stationary components within the turbine, particularly at full engine power and when the particles are relatively large. Since it is already established that such (adhering) VA can have highly deleterious effects within a turbine, on both short and longer timescales, this is clearly an issue of concern. Characterization of a VA known to be airborne in substantial quantities at a particular time and location, notably in terms of establishing its  $T_g$  and amorphous content, may be a useful practical measure.

Received: November 24, 2012

Final Version: April 24, 2013

Published online: June 25, 2013

- J. M. Drexler, A. D. Gledhill, K. Shinoda, A. L. Vasiliev, K. M. Reddy, S. Sampath, N. P. Padture, *Adv. Mater.* **2011**, 23, 2419.
- A. Hamed, W. Tabakoff, R. Wenglarz, *J. Propulsion Power* **2006**, 22, 350.
- K. Brun, M. Nored, R. Kurz, *J. Eng. Gas Turbines Power* **2012**, 134, 012402.
- W. Ai, T. H. Fletcher, *J. Turbomachinery* **2012**, 134, 041020.
- J. P. Bons, J. Crosby, J. E. Wammack, B. I. Bentley, T. H. Fletcher, *J. Eng. Gas Turbines Power* **2007**, 129, 135.
- J. M. Crosby, S. Lewis, J. P. Bons, W. Ai, T. H. Fletcher, *J. Eng. Gas Turbines Power*, **2008**, 130, 051503.
- J. P. Bons, R. Taylor, S. McClain, R. Rivir, *J. Turbomachinery – Transact. Asme* **2001**, 123, 739.
- X. Chen, *Surf. Coat. Technol.* **2006**, 200, 3418.
- M. P. Borom, C. A. Johnson, L. A. Peluso, *Surf. Coat. Technol.* **1996**, 87, 116.
- C. Mercer, S. Faulhaber, A. G. Evans, R. Darolia, *Acta Mater.* **2005**, 53, 1029.
- S. Kramer, S. Faulhaber, M. Chambers, D. R. Clarke, C. G. Levi, J. W. Hutchinson, A. G. Evans, *Mater. Sci. Eng. A* **2008**, 490, 26.

- [12] M. H. Vidal-Setif, N. Chellah, C. Rio, C. Sanchez, O. Lavigne, *Surf. Coat. Technol.* **2012**, 208, 39.
- [13] R. Wellman, G. Whitman, J. Nicholls, *Int. J. Refract. Metals Hard Mater.* **2010**, 28, 124.
- [14] M. Shinozaki, T. W. Clyne, *Acta Mater.* **2013**, 61, 579.
- [15] S. Kramer, J. Yang, C. G. Levi, C. A. Johnson, *J. Am. Ceram. Soc.* **2006**, 89, 3167.
- [16] M. Shinozaki, T. W. Clyne, *Surf. Coat. Technol.* **2013**, 216, 172.
- [17] D. J. de Wet, R. Taylor, F. H. Stott, *J. Phys. IV France* **1993**, 03, C9.
- [18] J. Wu, H-b. Guo, Y-z. Gao, S-k. Gong, *J. Eur. Ceram. Soc.* **2011**, 31, 1881.
- [19] J. W. Jensen, S. W. Squire, J. P. Bons, T. H. Fletcher, *J. Turbomachinery* **2005**, 127, 462.
- [20] J. P. Van der Walt, A. Nurickt, *J. Aircraft* **1995**, 32, 106.
- [21] A. Rozati, D. K. Tafti, S. S. Sreedharan, *J. Turbomachinery* **2011**, 133, 011010.
- [22] A. Shah, D. K. Tafti, *J. Turbomachinery* **2007**, 129, 816.
- [23] S. Shipley, A. M. Sarna-Wojcicki, U.S. Geological Survey Miscellaneous Field Studies Map MF-1435 **1983**.
-